Pitting corrosion of 17-4PH stainless steel manufactured by laser beam melting

Adrien Barroux, Nadège Ducommun, Eric Nivet, Lydia Laffont, Christine Blanc

Pitting corrosion of 17-4PH stainless steel manufactured by laser beam melting

Adrien Barroux[a,b], Nadège Ducommun[b], Eric Nivet[b], Lydia Laffont[a], Christine Blanc[a,*]

[a] CIRIMAT, Université de Toulouse, CNRS, INP-ENSIACET, 4 allée Emile Monso, BP 44362, 31030 Toulouse cedex 4, France
[b] CETIM, Pôle Matériaux Métalliques et Surfaces, 74 route de la Jonelière, CS 50814, 44308 Nantes, France

ARTICLE INFO

Keywords:
A. Stainless steel
B. Polarisation
B. TEM
C. Passivity
C. Pitting corrosion

ABSTRACT

The pitting corrosion behaviour of a 17-4PH martensitic stainless steel (MSS) manufactured by power bed laser beam melting (LBM) was compared to that of a wrought MSS. More noble pitting potentials were measured for LBM samples, probably due to a smaller size of NbCs as compared to wrought MSS. The metastable pits were less numerous, but had a higher nucleation rate and longer life time for the LBM samples compared to the wrought MSS. This was explained by assuming a decrease in the repassivation ability of LBM samples due to small gas pores.

1. Introduction

Precipitation hardening martensitic stainless steels (MSSs), e.g. 17-4PH, are commonly used in many industrial applications like nuclear power plants, aircraft components, chemical industries and biomedical tools because of a combination of high mechanical properties and a good corrosion resistance. Those properties are obtained after an ageing heat treatment, following a solution annealing heat treatment and quenching, the ultimate tensile strength and fracture toughness values being controlled by the temperature and duration of the ageing [1]. During the ageing, significant hardening occurs due to the precipitation of fine Cu-rich precipitates in martensitic laths [2–6]. However, other microstructural changes occur, i.e. an evolution of the martensite - austenite ratio, the growth of carbides and Cu-rich precipitates and the modification of the grain size [1,5–8]. The evolution of the 17-4PH microstructure during hardening heat treatment is well-known for the steel provided by conventional metallurgy and the relationship between the microstructure and the mechanical properties has been extensively studied [2–6,9–11]. However, it can be suspected that, for a given heat treatment, the microstructure obtained after laser beam melting (LBM) could be different from that of a wrought SS; therefore the correlation between a heat treatment commonly used for conventional metallurgy for one part, and the microstructure and mechanical properties for the other part, could be more complex with additive manufacturing processes.

Additive manufacturing has become one of the most innovative processes to build metallic components because it allows complex geometry parts to be created in a short time. LBM, which is a powder additive manufacturing process, is based on the use of a laser beam to melt locally a metallic powder and construct a 3D part layer by layer. The influence of the LBM process and the scan parameters on the microstructure and the mechanical properties has been well discussed in the literature for many types of materials [12–14]. The parameters to take into account during LBM process are numerous; for example, the nature of the initial metallic powder, the protective gas, the energy density of the laser and the scan strategy can generate different microstructures and create LBM specific defects, e.g. un-melted cavities and pores [15–18]. Concerning the 17-4PH, Murr et al. have studied the influence of the nature of the initial metallic powder and of the protective gas used during manufacturing of the LBM part on its microstructure [17]. The parts fabricated with argon or nitrogen-atomised powder under argon protective gas are mainly composed of martensitic phase, whereas those fabricated with nitrogen-atomised powder under nitrogen gas are mainly composed of austenite. In this last case, a high nitrogen content in the powder and the final part can be found leading to a stabilisation of the austenitic phase by lowering the martensitic start temperature (M_s) [2,18,19]. In addition, LBM 17-4PH MSSs has a specific microstructure induced by the process, which leads to morphological texture through the building direction of the parts with a dendritic microstructure. All these particular microstructural features lead to a complex mechanical response with significant differences depending on the loading axis during the mechanical test and the building direction of the as-built parts [15,19–25]. Heat treatments performed after the building step can also modify the microstructure;

* Corresponding author at: CIRIMAT, Université de Toulouse, CNRS, INP-ENSIACET, 4 allée Emile Monso - BP 44362, 31030, Toulouse cedex 4, France.
E-mail address: christine.blanc@ensiacet.fr (C. Blanc).

https://doi.org/10.1016/j.corsci.2020.108594

Table 1
Chemical composition of the wrought and LBM 17-4PH MSSs. The chemical composition of the powder used for the LBM MSS is also given.

Element wt. %	Cr	Ni	Cu	C	Nb	Mn	Si	Mo	N	Fe
wrought	15.42	4.49	3.24	0.036	0.26	0.39	0.35	0.15	0.030	bal.
LBM (powder)	16.14	3.95	3.67	0.037	0.27	0.35	0.64	≤ 0.02	0.030	bal.
LBM (bulk material)	16.20	4.08	3.56	0.028	0.27	0.32	0.71	≤ 0.02	0.035	bal.

results showed that the solution annealing and ageing heat treatment commonly used for conventional 17-4PH MSS, e.g. the H900 treatment (solution annealing heat treatment at 1040 °C during 30 min followed by an ageing at 480 °C during 1 h), reduces the morphological texture, homogenises the precipitation and induces a recrystallisation phenomenon [16,18]. Yet, the volume of austenitic phase obtained after the LBM process, which depends, as said previously, on the nature of the powder and of the protective gas as well as on the heat treatment applied after the building step, can be different from that obtained for a wrought alloy for the same heat treatment. These differences and the specific LBM process defects affect the ultimate tensile strength, elongation, and fatigue behaviour compared to a conventional MSS [16–18]. Mechanical behaviour and especially the crack initiation are associated to pores and un-melted cavities, which reduce the elongation to failure and fatigue life time. Oxide inclusions specifically generated by the LBM process in presence of oxygen could initiate and propagate cracks when mechanical stress is applied, and this impacts negatively the toughness and SCC properties [26–28].

Furthermore, microstructural changes due to the ageing heat treatment described before can also impact the corrosion behaviour of MSSs, and more precisely their susceptibility to pitting corrosion and intergranular corrosion; this has been shown for conventional SSs [29–32]. The pitting potential for these materials is closely linked with the chemical composition and structure (defects, grain boundaries…) of the passive film, which is strongly related to the microstructure of the substrate [33]. Moreover, mechanical defects like micro-cracks around inclusions can slightly decrease the pitting potential and increase the susceptibility to metastable pitting of the material [8,34]. In the case of additive manufacturing, there are only a few publications about the susceptibility to corrosion of austenitic SSs with different manufacturing processes [35–40]. For example, Chao et al. have shown a better resistance to pitting corrosion for a LBM austenitic SS compared to a wrought material [40]. The more positive values of pitting potential were explained by the finer microstructure due to high solidification rate. In particular, the MnS inclusions in the matrix had a smaller size in LBM SS compared to wrought material, which avoided Cr depletion and allowed an homogeneous passive film to be formed [40]. Another study has showed the importance of the powder atomisation gas on the pitting corrosion of austenitic SS and pointed out the effect of secondary alloying elements, e.g. Mn, present in the powder [41]. However, the corrosion mechanisms affecting the LBM MSSs and the influence of microstructure on their corrosion properties are not yet fully understood and further investigations on their corrosion behaviour are required.

In the present study, the pitting corrosion behaviour of a LBM 17-4PH MSS was compared to that of a wrought 17-4PH MSS, considering, for the LBM steel, different planes relative to the building direction. First, the microstructure of both the wrought and LBM MSSs was characterised at different scales to detect any significant differences between the two MSSs that could suggest changes in the corrosion behaviour of the 17-4PH MSS due to the LBM process. Then, the corrosion behaviour of the samples was studied by performing both potentiostatic and potentiodynamic electrochemical experiments. A statistical study of the metastable pits was performed to characterise the metastable pitting susceptibility of the steels. Finally, the results obtained from the electrochemical measurements on the one hand, and from the analysis of the microstructures for the other hand, were compared to better understand the corrosion behaviour of the LBM MSS.

2. Experimental procedure

The material studied corresponded to LBM parts fabricated from 17-4PH MSS nitrogen-atomised powder provided by Erasteel with an average diameter of 33 µm. Cubic LBM MSS parts of 20 × 20 × 20 mm^3 were produced in an EOS M290 machine equipped with a 400 W laser under argon atmosphere. During the process, the building plate was maintained at 200 °C. For each LBM cube, several planes were identified; XY plane corresponded to a plane parallel to the building plate and Z was the building direction. For comparison purposes, a conventional wrought 17-4 PH MSS provided by Böhler Edelstahl as a 50-mm cylinder was also studied as reference. In this work, samples were removed only from the core of the samples (cubes and cylinders) in order to compare the microstructure and the corrosion behaviour of the bulk material without considering any influence of the edges, e.g. the contouring strategy implemented by the LBM process. The chemical composition for the LBM bulk parts, the LBM powder and the wrought steel is given in Table 1; some slight differences are observed between LBM and wrought samples, in particular for the Cr, Ni and Cu content, but also for the Si content which is twice higher for the LBM MSS. Both samples, wrought and LBM, were solution annealing heat treated at 1040 °C for 30 min immediately followed by air quenching; then, they were aged at 480 °C for 1 h, which corresponded to the standardised H900 ageing. Moreover, in order to help ascertain the difference between the H900 wrought MSS and the H900 LBM MSS, but also to help with the development of a "database" within the literature, some results are given for the as-built LBM samples in supplementary material.

To analyse the microstructure of the MSSs, samples were mounted in an epoxy resin, ground using SiC papers down to 4000 grade, then polished down to mirror surface with 0.05 µm OPS particles, and finally chemically etched with Fry's reagent (40 mL HCl, 5 g $CuCl_2$, 25 mL EtOH and 30 mL H_2O). Observations of the microstructure were first carried out by using a MA200 Nikon Optical Microscope (OM) and a FEI Quanta450 Scanning Electron Microscope (SEM). Prior austenitic grain size was measured by applying the intercept method to OM images; 250-µm long lines (4 lines) were plotted to calculate the average grain size. The core porosity of the LBM MSS was evaluated by image analysis on a large image of 2732 × 919 $µm^2$. Pores under 0.5 $µm^2$ were not detected with this method. Transmission electron microscopy (TEM) was also used to complete the characterisation of the microstructure. Samples were cut and thinned close to 30 µm by mechanical grinding and polishing, and then electropolished by using a Tenupol-5 unit polisher with a 70 % ethanol, 20 % 2-butoxyethanol, 10 % perchloric acid solution under 14 V at 2 °C. TEM imaging was performed with a JEOL JEM 2100 F microscope operated at 200 kV and equipped with an Energy Dispersive X-ray Spectroscopy (EDS) analyser (Brucker SDD Xflash 5030). The diffraction patterns were recorded using selected area electron diffraction (SAED) mode with a 150 nm aperture or a digital diffraction pattern obtained by fast Fourier transform (FFT) of a high resolution TEM (HRTEM) image. A D8 Bruker diffractometer was used for preliminary X-Ray Diffraction (XRD) analyses, with a Cu anode ($K_{\alpha 1}$ at 1.5406 Å) source, in order to identify the nature of the metallurgical phases in the MSSs. In addition, in order to determine accurately the proportion of each phase, energy dispersive XRD analyses were also

performed by using a W anode at a 18.25° θ value between 12 keV and 40 keV. The same samples were used for both analyses and were only ground down to 1200 grade SiC before the measurements.

The corrosion behaviour of the MSSs was analysed by performing electrochemical experiments in a 0.5 M NaCl solution maintained at 25 °C, stirred and open to air with a three-electrode cell. A saturated calomel electrode (SCE) and a platinum foil were used as reference electrode and counter electrode, respectively. Samples were mounted into an epoxy resin with a Cu wire for electric connexion. Before each electrochemical measurement, the sample surface was mechanically ground with SiC paper down to 2400 grade, then polished with diamond paste down to 1 µm, and finally rinsed with deionised water in an ultrasonic bath. First, open circuit potential (OCP) measurements were performed by recording the OCP values every 10 s for 24 h. For each measurement, the OCP value after the 24 h immersion was then calculated by considering the values recorded during the 30 last minutes. These experiments were repeated three times for each sample; the values given further corresponded to the average values calculated from these three experiments. Before all the potentiostatic and potentiodynamic experiments, the samples were immersed at their OCP for 1 h in order to reach the near steady state conditions. The polarisation curves were plotted by sweeping the potential at 500 mV h^{-1} (8.3 mV min^{-1}) from the OCP to −500 mV versus SCE for the cathodic curves, and to a potential corresponding to a current density value equal to 100 µA cm^{-2} for the anodic curves; the surface exposed to the electrolyte was 2 cm^2. For the potentiostatic polarisations, samples with a 1-cm^2 surface were maintained at a constant potential of 100 mV versus SCE, i.e. in the passive range, in order to study the initiation of metastable pits. The current response was recorded for 1800 s with a measurement performed every 0.1 s. A value of 30 nA above the background current was chosen as the threshold to identify the current peaks characteristic of metastable pits. For the study of stable pits, a current of 1 mA was applied on 1-cm^2 samples for 10 min. The cathodic polarisation curves were repeated 3 times, the anodic curves 10 times and current-time curves 5 times for each sample in order to provide a statistical study. After the electrochemical measurements, the corroded surfaces were observed by using OM and SEM to analyse the corrosion features. In order to determine the morphology and size of the pits, a S Neox Sensofar confocal and interferometric microscope was used. It allowed the roughness of the surface to be measured after the electrochemical tests, resulting in topological maps of the samples, where pits were identified. Values characteristic of the pit morphology (depth, diameter) were extracted from the mean profiles of the pits.

3. Experimental results and discussion

3.1. Study of the microstructure of the 17-4PH MSSs

Core microstructures of the LBM and wrought 17-4PH MSSs heat treated following the H900 ageing characteristics were observed by using OM after chemical etching with Fry's reagent (Fig. 1). OM micrographs show a similar microstructure for wrought and LBM samples with martensitic laths in equiaxed prior austenitic grains. The grain size was slightly smaller for LBM MSS (9.7 ± 0.7 µm for XY plane and 9.9 ± 0.8 µm for XZ plane) than for wrought MSS (12.8 ± 1.0 µm). For both materials, the microstructure was homogeneous, which was, at least partially, due to the recrystallisation process induced by the solution annealing heat treatment at 1040 °C. For the planes XY (parallel to the building plate) and XZ (parallel to the building direction) of the LBM samples, there was no evidence of the scan pattern on the microstructure, i.e. melt pools for XZ plane or laser passes for XY plane, contrary to what was observed for the as-built LBM samples (Fig. A in the supplementary material). Furthermore, it was of major importance to note here that the total porosity of the LBM samples was evaluated to be around 0.04 % only, so that very few defects characteristic of the LBM process, i.e. spherical gas pores and lack-of-fusion pores, were observed. Pores in the LBM samples were found to be mainly small gas pores (around 1 µm). Only very few lack-of-fusion pores could be found; they were bigger than gas pores (around 10 µm). This showed that optimised parameters for the LBM process allowed samples of very high density to be produced, in agreement with Laleh's results [42]. The XRD patterns plotted for both wrought and LBM MSSs are shown in Fig. 2. XRD patterns confirmed the mainly martensitic microstructure for all the samples with body cubic centred (bcc) structure (α'-Fe, space group Im-3 m, a = 2.87 Å). The bcc structure of the martensite was explained by the low carbon content of the MSS: carbon was rejected from the martensitic matrix during the ageing heat treatment leading to a transition from the tetragonal structure to bcc structure [1]. A secondary austenitic phase with face centred cubic (fcc) structure (γ-Fe, space group Fm-3 m, a = 3.59 Å) was also detected for the LBM material only. Results of phase quantification obtained by energy dispersive XRD are given in Table 2. For the wrought 17-4PH MSS, only a very small amount of austenitic phase was detected. On the contrary, LBM material contained a non-negligible amount of austenitic phase, with 12 % of austenitic phase detected for XY plane, and only 8% for XZ and YZ planes. These differences between XY plane from one part, and XZ and YZ planes from the other part, could be related to the anisotropic morphology of the prior austenitic grains observed before the H900 heat treatment (Fig. A in the supplementary material). It could be noted that no austenitic grain was identified by using OM for the H900 samples; this suggested that those grains were too small to be observed by OM.

SEM images of the wrought and the LBM XY steels after chemical etching are shown in Fig. 3. The images highlighted the presence of spherical-shape precipitates identified as Nb carbides (NbC) by using EDS. They were found all over the samples, especially at grain boundaries but also in the packets of martensite laths. A qualitative analysis led us to assume that the density of NbCs was similar for the

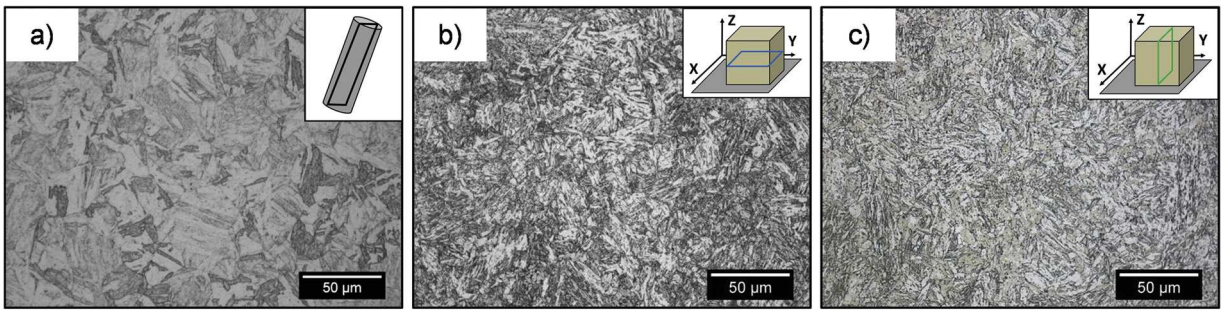

Fig. 1. OM observations of a) wrought, b) LBM XY, and c) LBM XZ samples after chemical etching with Fry's reagent. The wrought samples were removed from the core of a 50-mm cylinder; OM observations were done on a plane parallel to the cylinder axis (insert in Fig. 1a). Inserts in Fig. 1b and c are for LBM samples: in grey, the building plate on which the LBM samples (cubes) are built. The blue (insert in Fig. 1b) and green (insert in Fig. 1c) squares show the planes observed by using OM. (For interpretation of the references to colour in this figure legend, the reader is referred to the web version of this article).

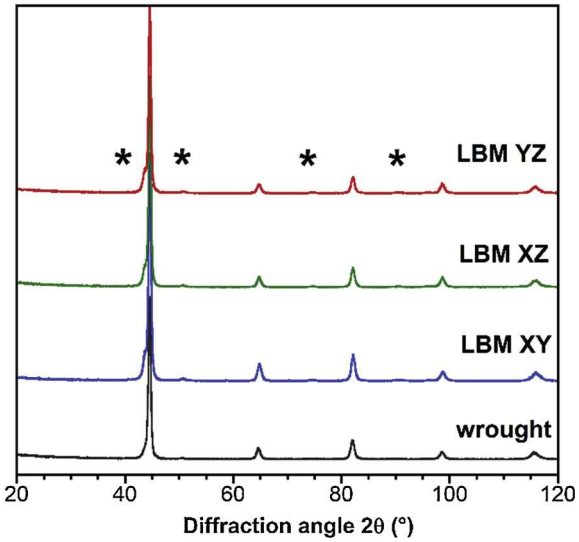

Fig. 2. XRD patterns plotted for the different 17-4PH samples (peaks with * correspond to the austenitic phase).

Table 2
Quantification of phases obtained by Energy dispersive XRD analyses.

	α' phase (wt. %)	γ phase (wt. %)	Standard deviation on γ (%)
wrought	99.2	0.8	0.2
LBM XY	87.4	12.6	0.3
LBM XZ	91.7	8.3	0.2
LBM YZ	91.5	8.5	0.2

wrought and LBM steels. These NbC precipitates are known to have fcc structure (space group Fm-3 m, a = 4.4 Å) with $M_{23}C_6$ or M_7C_3 stoichiometry and participate to the hardening of the MSS [6,27,39]. At the SEM scale, NbC precipitates seemed to be smaller in LBM XY steel than in wrought material. Bright field TEM overview images (Fig. 4) of wrought (Fig. 4a) and LBM XY (Fig. 4b) MSS showed packets of martensite laths (same lath orientation) with NbC in the laths or at lath boundaries. In the wrought MSS, NbC precipitates were coarser around 1 µm and had an elliptic shape, by comparison to the NbC observed in the LBM XY MSS that were less than 500 nm in diameter and had spherical shape. Attention was also paid to Si-rich oxide inclusions found at nanoscale in the LBM samples (Fig. 4b and f). The Si-rich oxide inclusions were not detected in wrought MSS; they were formed during the LBM production process despite the use of protective gas. Such inclusions, considered as manufacturing defects, were characterised by several authors on a 316 L stainless steel produced by LBM [27,28]. Then, SAED pattern (Fig. 4a) was performed with a 150 µm aperture on martensite laths for the both materials, which confirmed the bcc structure of the martensite (a = 2.868 Å). The martensite laths were found to be finer for LBM XY MSS (between 50 and 800 nm) than for the wrought MSS (between 700 nm and 2.5 µm). The bright field TEM images also showed fine Cu-rich precipitates (CRPs) in the martensitic laths for wrought (Fig. 4c) and LBM XY (Fig. 4d) MSSs. This observation was consistent with the literature [2–6] that showed that an ageing heat treatment H900 generated CRPs in the martensitic matrix, leading to an increase in the hardness values. As expected, these CRPs had a bcc structure (CRPs, space group Im-3 m, a = 3.026 Å) and were therefore coherent with the martensitic matrix. A HRTEM image focused on a CRP is shown in Fig. 4e for LBM XY sample; it showed that the CRPs had elliptic shape and were around 10 nm in diameter as expected [2,5,6]. CRPs were difficult to find and to be observed in the wrought MSS certainly due to a lower precipitate content or a smaller size. Such a difference could be related to the Cu content. Austenitic grains were also observed (Fig. 4f) at boundaries of martensitic laths for LBM XY

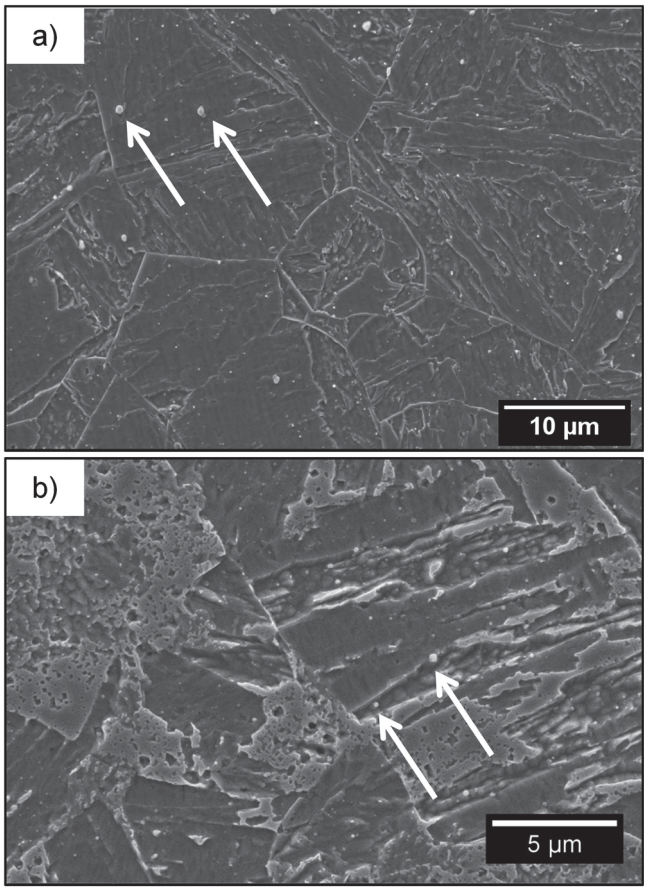

Fig. 3. SEM micrographs of a) wrought, and b) LBM XY samples after chemical etching with Fry's reagent. White arrows show NbC carbides.

sample; they were characterised by a fcc structure (a = 3.59 Å), in agreement with the XRD results. As previously assumed from OM and SEM observations, the austenitic grains were found to have a very small size with the same chemical composition (measured by EDS) as the martensitic matrix. These results led us to assume that those grains corresponded to retained austenite, which had not been transformed during the ageing. Clearly, this made it more complex to observe austenitic phase in the 17-4PH samples.

The results described above showed non-negligible differences in the microstructure between the wrought and LBM MSSs. Further, some differences were also detected between the different planes of the LBM sample. It was therefore of interest to determine whether those differences could have a significant influence on the corrosion behaviour of the samples.

3.2. Corrosion behaviour of the 17-4PH MSSs

3.2.1. Electrochemical behaviour

The corrosion behaviour of both wrought and LBM MSSs was first evaluated by measuring the OCP. OCP curves plotted for 24 h in 0.5 M NaCl are shown in Fig. 5a for all samples. Results showed a similar evolution of the OCP for the wrought MSS and the different planes of the LBM MSS. In the early stages of immersion, for both samples, a sharp increase of the OCP was observed due to the evolution and growth of the passive film. Then, after about one hour of immersion, the curves were characterised by a slower increase of the OCP, for all the samples. However, the results clearly showed that the wrought MSS rapidly reached steady state conditions, whereas a higher variation of the OCP was observed during the 24 h immersion for the LBM MSS; LBM samples did not reach the steady state conditions after 24 h.

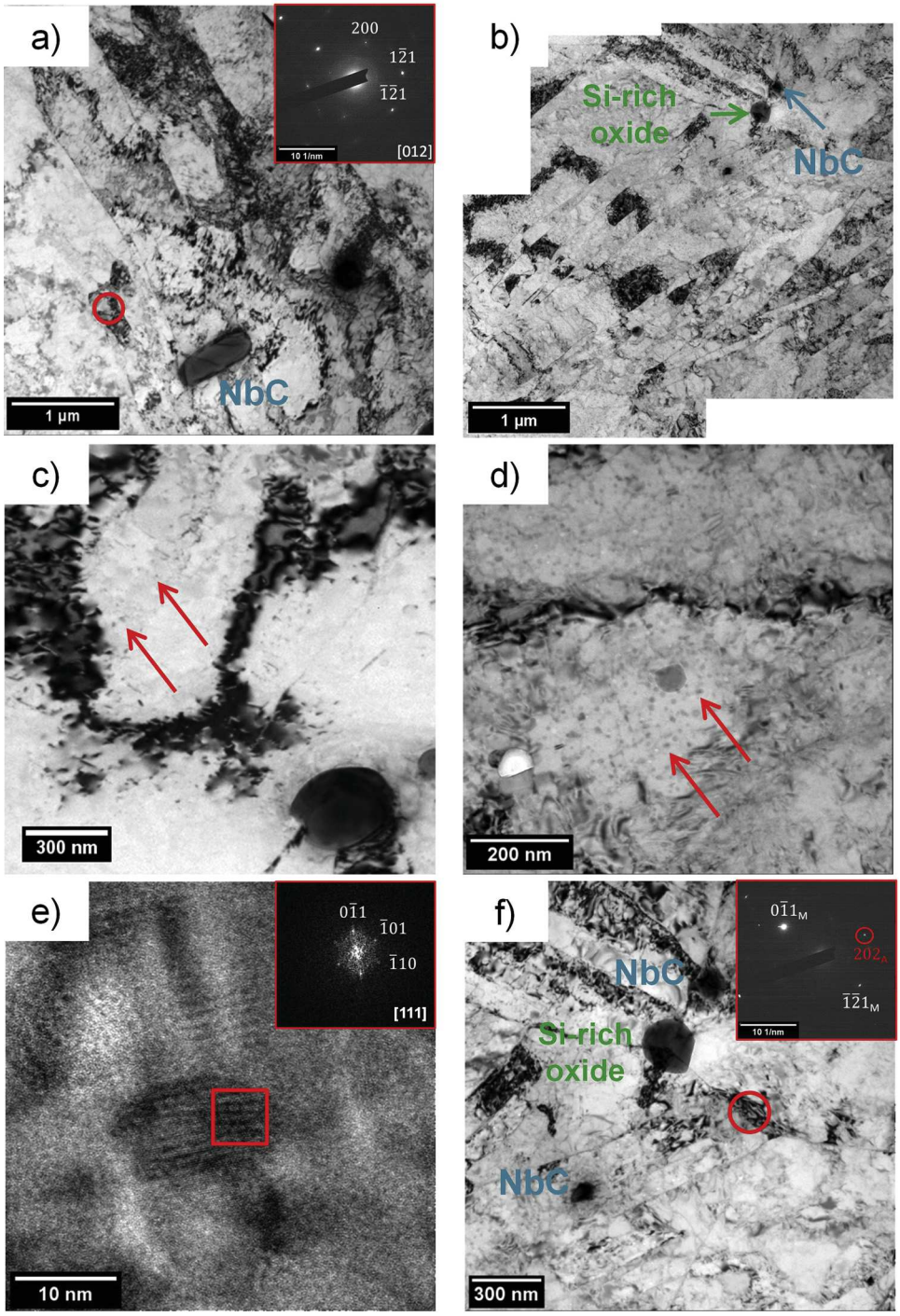

Fig. 4. Bright field TEM images of the wrought and LBM XY 17-4PH MSSs: low magnification with an overview of the martensite laths and some NbC precipitates for a) wrought, and b) LBM XY; some Cu-rich precipitates (red arrows) of c) wrought, and d) LBM XY samples; e) HRTEM image of Cu-rich precipitate for LBM XY sample; f) bright field image of LBM XY sample showing residual austenite at a lath boundary (red circle), NbC precipitates and a Si-rich inclusion. Inserts in Fig. a), f) correspond to selected area electron diffraction obtained with a 150 nm aperture (red circles) and e) to a digital diffraction pattern (red square) obtained by FFT of the HRTEM image of a Cu-rich precipitate. (For interpretation of the references to colour in this figure legend, the reader is referred to the web version of this article).

Nevertheless, no corrosion defects such as pits were detected after a 24 h immersion in 0.5 M NaCl for both MSSs, demonstrating the passive state of the MSSs at OCP. Therefore, the results suggested only that some differences in the properties of the passive films might be expected.

Potentiodynamic polarisation curves plotted in the same electrolyte are shown in Fig. 5 b and c for cathodic range and anodic range, respectively. A one-hour OCP measurement was performed before either cathodic or anodic polarisation curves to reach the near steady state conditions before the polarisation. For all samples, the cathodic curve was characterised by a well-marked current density plateau corresponding to the diffusion-controlled reduction reaction of dissolved oxygen; the cathodic current densities were similar for all the samples.

The anodic curves showed a similar shape for all the samples, with a passivity plateau followed by a sudden increase of the anodic current densities for positive potentials in the [0.2–0.3] $V_{/SCE}$ range. OM observations of the samples after the polarisation tests (not shown here) showed numerous pits on the MSS surface, which evidenced that the passivity breakdown was related to pitting corrosion. Moreover, current transients were also observed before the pitting potential (E_{pit}) for all samples; they were related to the formation of metastable pits. A first analysis, based on the observation of the polarisation curves, showed that there were more metastable pits for the wrought MSS compared to LBM samples. The average OCP values measured after 24 h of immersion are summarised in Table 3; as explained in the experimental part, they were calculated from 3 OCP measurements for each sample. The

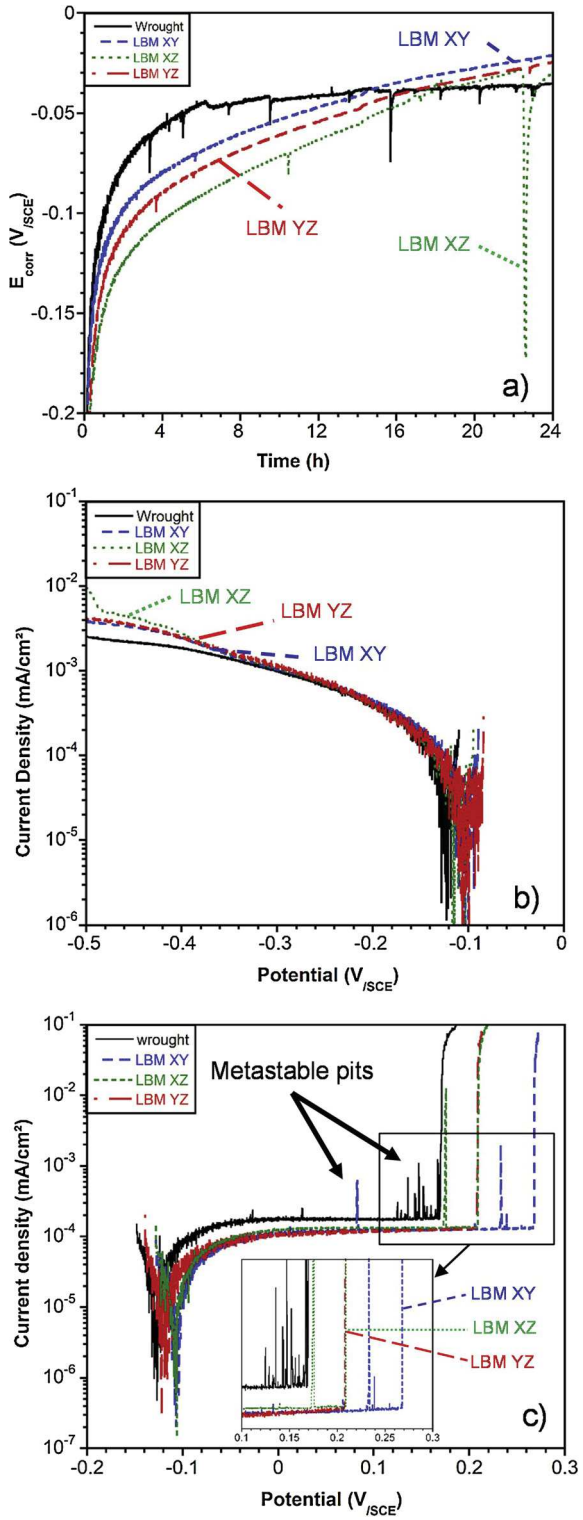

Fig. 5. a) OCP versus immersion time; b) cathodic and c) anodic parts of the potentiodynamic polarisation curves. All measurements were performed in 0.5 M NaCl, for the wrought and LBM samples. Insert in Fig. 5c allows to show that E_{pit} values are similar for LBM XZ and LBM YZ samples.

average values of the OCP after 1 h of immersion, as well as those of E_{pit}, i_{corr} and $i_{-0.3\ V/SCE}$ extracted from the polarisation curves, are also given, where i_{corr} was the corrosion current density, and $i_{-0.3\ V/SCE}$ the current density at a potential of – 0.3 $V_{/SCE}$. It could be noticed that the corrosion kinetics was controlled by the resistance of the passive films so that the passivity current density, i_{pass}, was equal to i_{corr}. All these average values were calculated on the basis of at least 10 measurements. After 1 h of immersion, no significant difference in OCP values (E_{corr} at 1 h) could be noticed between the wrought and the LBM MSSs. The same conclusions could be drawn for the OCP values measured after 24 h of immersion (E_{corr} at 24 h). The current densities in the cathodic domain were also very similar for all samples. However, more positive E_{pit} values and lower i_{corr} (i.e., i_{pass}) values were measured for the LBM samples compared to the wrought sample. These results suggested a better corrosion behaviour for the 17-4PH MSS manufactured by LBM than for the wrought one for the same heat treatment (H900). Furthermore, results also showed that the E_{pit} value was slightly more positive for the XY plane than for the (X,Y)Z planes of the LBM sample, whereas no significant difference in i_{corr} was measured between the different planes of the LBM MSS. Comparison of the polarisation curves plotted for the LBM samples after the H900 heat treatment with those plotted for the as-built LBM samples (Fig. B in the supplementary material) showed higher i_{pass} values, but more positive E_{pit} values for the as-built samples as compared to the LBM samples after the H900 heat treatment. Furthermore, a more positive E_{pit} value was measured for the XY plane, as compared to the XZ plane, for the as-built sample. Such comparison clearly showed the influence of the heat treatment on the corrosion behaviour of the LBM samples, and confirmed also the influence of the microstructure, depending on the sample orientation, on the pitting resistance of the LBM MSS. Considering those results, attention was paid successively to stable and metastable pitting for both the wrought and LBM samples after the H900 heat treatment.

3.2.2. *Study of the stable pits*

To better evaluate the susceptibility to pitting corrosion of the 17-4 PH MSS depending on the forming process, stable pits were first characterised: a current density of 1 mA cm^{-2} was applied on 1-cm^2 samples in order to compare both the density and morphology of the stable pits, for a similar charge passed for the different microstructures. Indeed, recent work of Clark and its co-workers demonstrated the nobility of NbC precipitates in austenitic stainless steels [43]. The authors suggested that NbC precipitates were cathodic with respect to the matrix and could create a micro galvanic couple promoting the initiation of localised corrosion. The differences in NbC size between the LBM and wrought samples could therefore have an influence on the stable pit initiation step, leading to differences in stable pit density between both LBM and wrought samples, and therefore, for a similar charge passed, to changes in the stable pit size. In a similar way, despite the very low amount of pores detected inside the LBM samples, those defects were also susceptible to affect the stable pit initiation process as shown in literature [44,45]. Therefore, it was of great interest to determine whether differences in pit density and/or size could be observed between wrought and LBM samples.

Global SEM observations of the pits are shown in Fig. 6 for the wrought sample (a) and the LBM XY sample (b). Different pit morphologies were observed, which were more or less spherical, but with no specific difference between the LBM and wrought samples. To go further in the pit description, the pit morphology was analysed by using a confocal microscope and plotting topological maps as shown in Fig. 7a. Morphological parameters such as the pit depth and diameter were measured (Fig. 7b); because of the drop-shape of the pits, two diameters were measured, i.e. the aperture diameter, that corresponded to the diameter measured on the sample surface, and the total diameter corresponding to the maximum diameter inside the pit. Mean values of those parameters are given in Table 4 for the wrought, LBM XY and LBM XZ samples (measurements were not done for the LBM YZ sample due to its similar corrosion behaviour as compared to LBM XZ sample). The total number of pits formed during the electrochemical tests is also indicated. Results showed that, despite the more positive E_{pit} values measured for the LBM samples, no significant differences could be found between the wrought, the LBM XY and LBM XZ samples considering the morphological parameters characteristic of the stable pits.

Table 3
Values of the corrosion parameters extracted from potentiodynamic polarisation and OCP curves.

	E_{corr} at 1 h ($mV_{/SCE}$)	E_{corr} at 24 h ($mV_{/SCE}$)	E_{pit} ($mV_{/SCE}$)	$I_{corr} = I_{pass}$ (nA cm^{-2})	$I_{0.3V/SCE}$ (nA cm^{-2})
wrought	−131 ± 3	−17 ± 17	170 ± 25	243 ± 93	−1104 ± 154
LBM XY	−111 ± 8	−18 ± 18	272 ± 32	109 ± 28	−1239 ± 188
LBM XZ	−102 ± 11	−39 ± 33	238 ± 72	107 ± 33	−869 ± 184
LBM YZ	−107 ± 13	−36 ± 30	248 ± 66	115 ± 42	−891 ± 230

.

Then, previous SEM observations of the samples surface were completed by SEM observations of the bottom of the pits (Fig. 6c and d). Results showed that, for the 17-4PH MSS, independent of the forming process, the pit propagation was dependent on the microstructure. This could be associated to the lower pH at the bottom of the pits, due to the anodic reactions and subsequent hydrolysis of the cations. Such an acidic electrolyte led to the preferential dissolution of both the grain boundaries and the matrix surrounding the NbCs. Therefore, these observations could suggest that NbCs might act as preferential pit initiation sites, as demonstrated by Clark and its co-workers [43]. However, considering the very small size of the NbCs, it was not trivial to establish a clear relationship between pit initiation and NbCs. Nevertheless, the less positive E_{pit} values measured for the LBM samples after the H900 heat treatment as compared to as-built LBM samples might be considered as an indirect experimental proof of the NbC detrimental role on the pitting corrosion resistance of LBM samples. Indeed, for the LBM samples after the H900 heat treatment, the solution annealing heat treatment at 1040 °C might have induced an increase in the amount of NbCs as compared to the as-built samples. Therefore, the measurement of a less noble E_{pit} for the LBM H900 samples as compared to the as-built samples (Fig. B in the supplementary material) might confirm a detrimental role of the NbCs on pit initiation. However, the amount of NbC precipitates was not determined quantitatively, and this constitutes a difficult task considering, as said previously, the size of the precipitates. Nevertheless, such an hypothesis should be in agreement with the conclusions drawn by Laleh et al. who showed a decline in pitting corrosion resistance of SLM 316 L SS after high-temperature post-processing, due to the formation of deleterious MnS inclusions [46]. Furthermore, comparison of E_{pit} values between the wrought and the LBM samples, both in the H900 metallurgical state, seemed to confirm also the deleterious influence of NbCs, with more noble E_{pit} values for LBM samples characterised by smaller NbCs as compared to the wrought MSS. Going back now to the similar pit size and density measured on both H900 LBM and wrought samples after polarisation with a similar current density (Fig. 7 and Table 4), such a result could be related to non-significant difference in the amount of NbCs present in both MSSs. Therefore, comparison of the results obtained from the polarisation curves for one hand, and for the polarisation with a fixed current density for the other hand, suggested that bigger NbCs could promote pit initiation more efficiently than smaller ones, but, once a pit was initiated, there was no significant effect of the NbC size. This could be explained also by considering that, despite the differences observed concerning some metallurgical parameters, e.g. the austenite content, the microstructure of the two MSSs was, from a global point of view, similar, which could explain that, once initiated and big enough, a pit propagated in a similar way for the two steels, leading then to the same

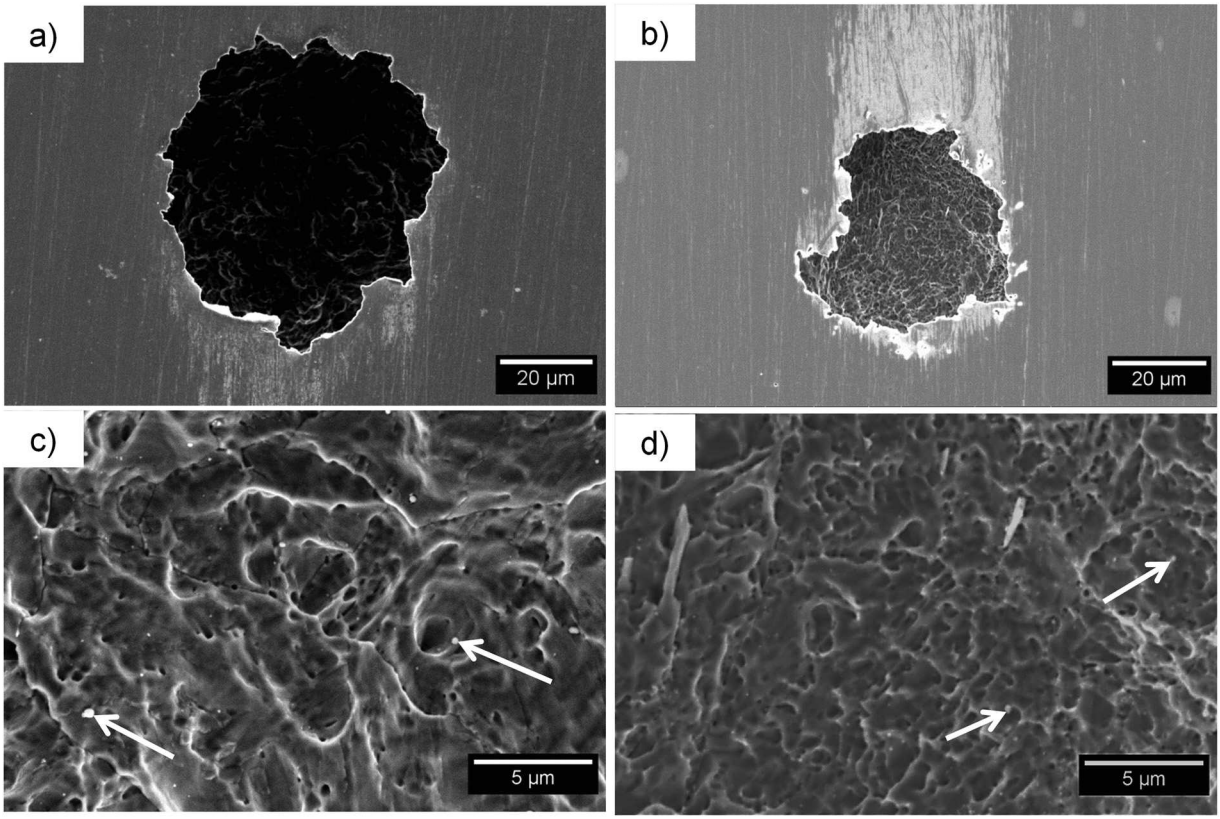

Fig. 6. Morphology of the stable pits formed in 0.5 M NaCl solution (current density applied of 1 mA cm^2 on 1-cm^2 sample for 10 min) for a) - c) wrought sample, b) - d) LBM XY sample. The arrows show the NbC precipitates, acting as preferential pit initiation sites.

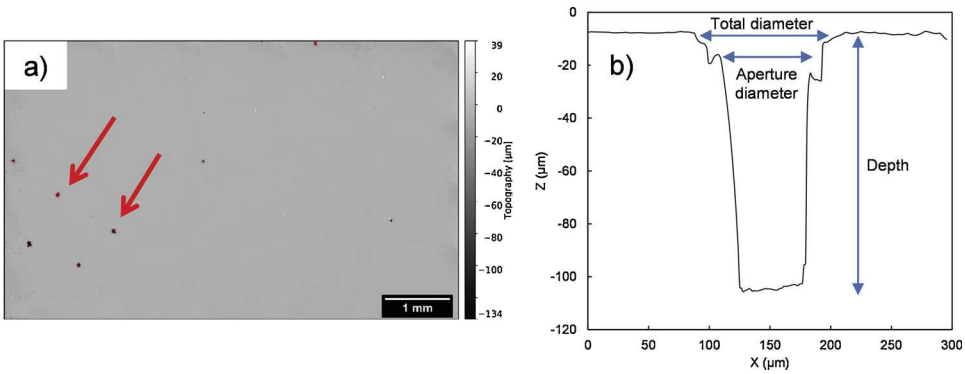

Fig. 7. a) Topological map plotted for the corroded wrought MSS by using a confocal microscope (current density applied of 1 mA cm^2 on 1-cm^2 sample for 10 min in 0.5 M NaCl). White arrows show the pits formed. b) Profile plotted for one pit.

Table 4
Parameters describing the pit morphology (number, size).

	Number of pits	Depth (µm)	Aperture diameter (µm)	Total diameter (µm)
wrought	17	87 ± 24	73 ± 17	114 ± 30
LBM XY	14	85 ± 12	64 ± 22	102 ± 26
LBM XZ	13	97 ± 17	60 ± 20	92 ± 28

density and same morphology for the pits. Nevertheless, the influence of those metallurgical parameters, in particular the austenite content, on the pitting resistance of LBM samples remained an unresolved issue that required much more detailed study. Furthermore, attention had to be paid to the influence of pores on the pitting behaviour of the LBM samples, many authors having demonstrated their detrimental effect on the pitting resistance [44,45]. However, in the present study, such an analysis was made very difficult due to the very low amount of pores. OM observations of gas pores before and after the polarisation tests at a fixed current density (Fig. 8a and b, respectively) showed that there was no clear evidence of a relationship between the gas pores present in the LBM steel and the pit initiation. This was in agreement with Laleh et al. who showed that the critical condition for pit initiation was not easily established for gas pores because they were open to the solution [45]. On the contrary, lack-of-fusion pores, with a very irregular shape, could lead to occluded volume favourable to pit initiation [44,45]. Observations of a lack-of-fusion pore before (OM, Fig. 8c) and after (SEM, Fig. 8d) the polarisation tests clearly showed that those defects promoted pit initiation. However, considering all the experiments performed for LBM samples, only one pit was observed in the surroundings of a lack-of-fusion pore, which was easily explained by considering that only very few lack-of-fusion pores were present in the LBM samples studied here. Therefore, even though our work confirmed the detrimental effect of lack-of-fusion pores on the pitting resistance of the SS,

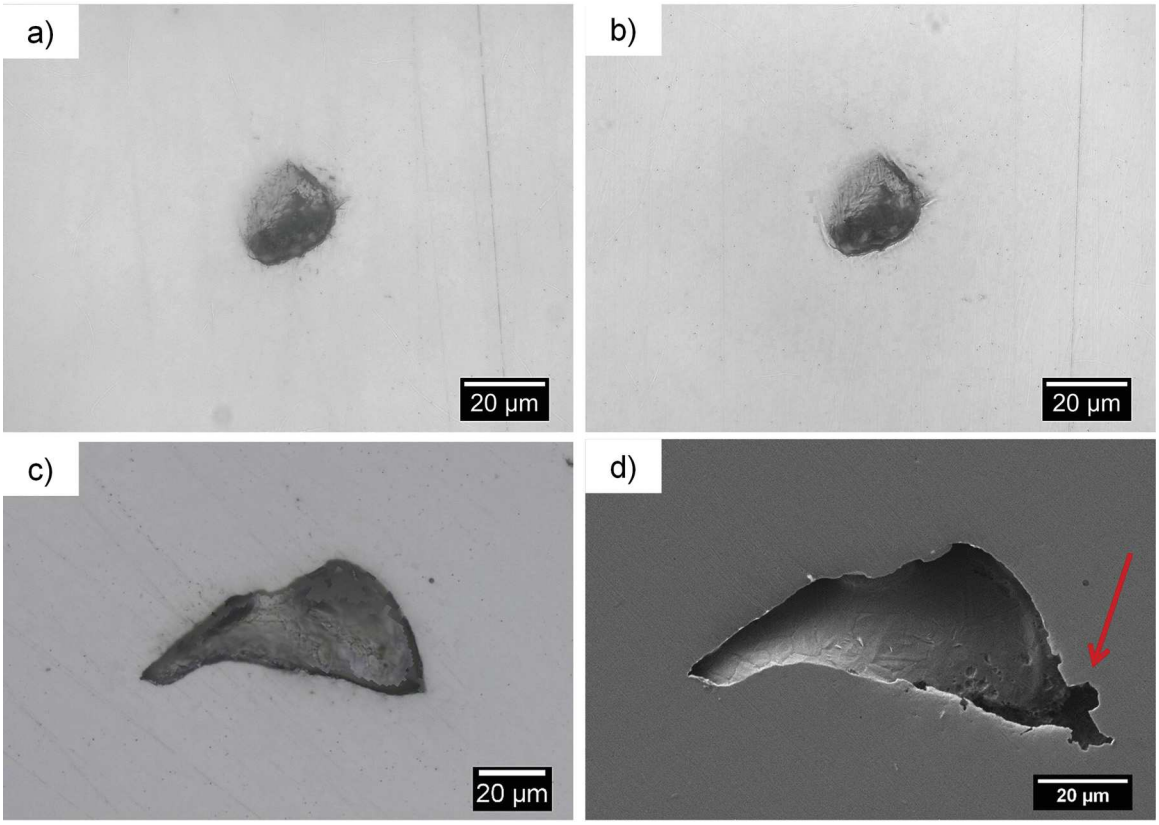

Fig. 8. OM observations of a gas pore a) before and b) after anodic polarisation in 0.5 M NaCl for LBM XZ MSS. c) OM observations before anodic polarisation of a lack-of-fusion pore for LBM XY MSS sample; d) SEM observation of a pit formed at the lack-of-fusion pore shown in c) after the anodic polarisation. The arrow shows the pit.

there was no significant effect of those defects on the stable pitting behaviour of the LBM MSS studied here due to a very low amount of those defects. Such a conclusion was in agreement with the literature who showed an improvement in pitting corrosion resistance for a SLM-produced 316 L SS as compared to a commercial counterpart [40,42]. The authors explained the results by the elimination, or the refinement of MnS inclusions in the SLM samples, whereas no influence of pores was observed on the pitting corrosion behaviour of the SLM samples due to their very low amount (a few small gas pores but no lack-of-fusion pores).

Therefore, it was concluded that the LBM and wrought 17-4PH MSSs had similar behaviour concerning stable pitting in terms of stable pit propagation and final shape. However, the difference in the E_{pit} values (Table 3) and the higher number of metastable pits observed on the polarisation curves for the wrought MSS (Fig. 5c) suggested non negligible differences in the protective properties, i.e. the stability, of the passive films grown on the two steels. This was consistent with the OCP measurements (Fig. 5a) that suggested differences in the evolution of the passive films formed for the two MSSs during the immersion in the NaCl solution. In order to validate this assertion concerning a difference in the protective properties of the passive films between the wrought and the LBM MSSs, the susceptibility to metastable pitting of the two MSSs was evaluated, and for more robustness of the results, a statistical analysis was performed.

3.2.3. Statistical study of the susceptibility to metastable pitting

In order to evaluate the susceptibility to metastable pitting of both MSSs in the H900 metallurgical state, potentiostatic polarisation tests were performed at + 0.1 $V_{/SCE}$ on 1-cm^2 samples in 0.5 M NaCl solution, after a 1 h immersion at the OCP. Such a methodology allowed to study the metastable pitting with a passive film formed (and not being formed) and in the near steady state conditions. Furthermore, considering the scattering of E_{pit} values, commonly observed for pitting corrosion, it was more relevant to perform the experiments at a fixed potential considering the OCP value rather than choosing a fixed potential below E_{pit}. To strengthen the results, the tests were repeated 5 times for each sample. Typical current versus time curves obtained by performing those potentiostatic tests are plotted in Fig. 9a for all 17-4PH MSSs. For all samples, the global shape of the curve was similar, with a fast decrease in the current values during the first 100 s of the experiments, which was related to the formation of the passive film on the sample surface. At the end of the potentiostatic polarisation tests, i.e. after 1800 s, the current reached a threshold value equal to the passivity current (i_{pass}); it could be noticed that the i_{pass} values measured with these potentiostatic experiments were in the range [100–200] nA cm^{-2} for all MSSs, which was in good agreement with the values extracted from the anodic polarisation curves (Fig. 5c). The duration time required to observe the stabilisation of the current on the current versus time curves (Fig. 9b) could be associated to the growth time of the passive film at the fixed potential; when the current was stabilised, there was an equilibrium between both dissolution and formation of the passive film. Numerous current transients were clearly visible on the current versus time curves. Considering the i_{pass} values, those transients were considered as characteristic of metastable pits when they reached a minimum current value of 30 nA (above the background current, for a 1-cm^2 surface studied). They could be described as a slow increase in the current, which corresponded to the growth of the metastable pit, followed by a current decay with a return to the background current value, which was related to the repassivation of the metastable pit. For metastable pits, as well as for stable pits, two steps can be considered, i.e. a nucleation step followed by a growth step controlled by the diffusion of the ionic species [47,48]. However, in the case of metastable pits, it is considered that the ions diffusion stay under a critical value, insufficient to generate a salt film at the bottom of the pit, which leads to repassivation. Considering the 5 potentiostatic polarisation tests performed for each sample, the total number of metastable pits formed was equal to 164, 33, 33 and 45 for the wrought, the LBM XY, LBM XZ and LBM YZ MSSs, respectively. This showed that there were significantly more metastable pits formed for the wrought sample than for LBM samples, in agreement with the conclusions drawn from the anodic polarisation curves (Fig. 5c).

Several parameters describing the current transients were then extracted from the curves in order to characterise the metastable pits, i.e. the current intensity I_{pit}, the charge amount Q_{pit}, the growth time T_g and the repassivation time T_r (Fig. 10). I_{pit} was the maximum value that the current transient could reach before going down to the background current and Q_{pit} corresponded to the surface area under the peak, i.e. the current transient. Moreover, the life time of the current transient was composed of T_g and T_r, those two parameters corresponding to the two characteristic steps of a metastable pit: T_g was the time for the current to reach I_{pit}, and T_r was the time for the current to go down to the background current value. The growth rate of the metastable pit was defined as the ratio (I_{pit} / T_g). Because of the probabilistic characteristic of the metastable pitting, a statistical approach was used to analyse those parameters. For each of them, a cumulative function (P(E)) was defined, where E was the studied parameter. To use this function, all the E values were ranked in increasing order of value. The probability of the n^{th} value was calculated as indicated by Eq. 1 [8,34,49]:

$$P(E) = \frac{n}{N+1} \quad (1)$$

where N was the total number of metastable pits, i.e. the total number of values. Based on this approach, cumulative probability curves were

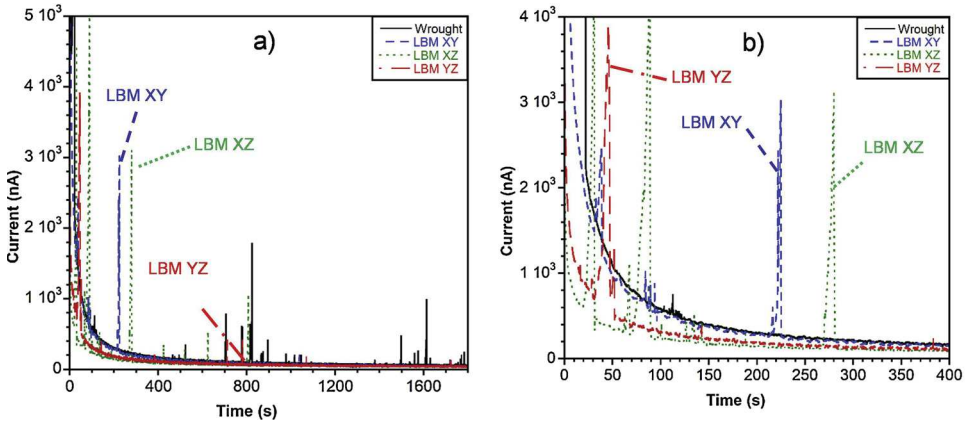

Fig. 9. a) Current versus time curves obtained after a 1 h immersion at OCP in 0.5 M NaCl. Potential applied = +100 $mV_{/SCE}$; b) focus on the first times of measurement.

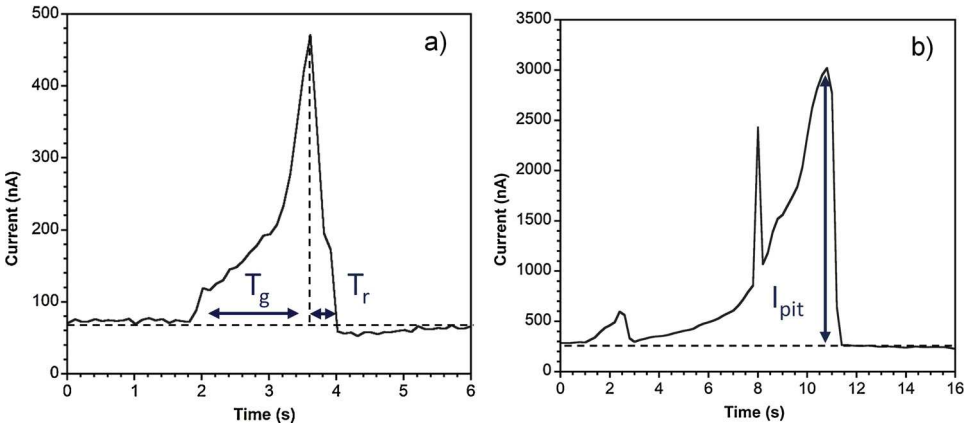

Fig. 10. Current transients corresponding to metastable pits for a) the wrought MSS, and b) LBM XY MSS.

Table 5
Median values of the parameters representative of the metastable pits. Values are extracted from the current versus time curves.

	I_{pit} (nA)	Q_{pit} (nC)	T_g (s)	T_r (s)	I_{pit} / T_g (nA/s)
wrought	133	90	1.1	0.2	148
LBM XY	329	211	1.6	0.4	214
LBM XZ	310	415	3.2	0.4	160
LBM YZ	344	334	2.6	0.4	185

plotted. The only values extracted from those curves were the median values (Table 5), in order to illustrate the comments; however, one must be careful with the meaning given to these numerical values. The cumulative probability curves of I_{pit} and Q_{pit} are shown in Fig. 11 for the wrought and LBM samples. As showed by the plots, these curves had the same shape. A significant difference could be observed between wrought and LBM samples, but a less marked difference could be also noticed between LBM XY sample and LBM (X,Y)Z samples. Results clearly showed that the metastable pits formed on the LBM XZ and YZ samples corresponded to both higher current intensity and higher amount of charge than metastable pits grown on LBM XY sample, and even more than those formed on the wrought MSS. This could be seen also by considering the median values of I_{pit} and Q_{pit}, even though there was not a significant difference in the I_{pit} values obtained for the 3 LBM samples. Moreover, another parameter was calculated for each sample, i.e. Q_{total}, which corresponded to the sum of the Q_{pit} values measured during the 5 tests: Q_{total} was found to be equal to 132, 307, 1650 and 3414 μC for the wrought, LBM XY, LBM XZ and LBM YZ samples, respectively. Those values were in good agreement with the I_{pit} and Q_{pit} values, with a total amount of charge corresponding to metastable pits significantly lower for the wrought MSS compared to LBM MSSs, despite a higher number of metastable pits formed on the wrought MSS; furthermore, the difference in metastable pitting behaviour between the LBM XY sample and the LBM (X,Y)Z samples was again clearly visible. Fig. 12 shows the cumulative probability curves plotted for T_g (Fig. 12a), T_r (Fig. 12b) and the growth rate (I_{pit} / T_g) (Fig. 12c), for all MSSs. The curves had a similar shape as those plotted for I_{pit} and Q_{pit}. Furthermore, the results showed that the metastable pits formed on the wrought MSS had a shorter life time than those formed on LBM MSSs. Moreover, as already observed with I_{pit} and Q_{pit} parameters, the LBM XY MSS clearly had a different reactivity than the other LBM samples, with a shorter life time of the metastable pits formed on the surface of the LBM XY sample compared to LBM XZ and YZ samples. This was visible also by considering the median values, in particular those of T_g. The specific reactivity of the LBM XY sample was also evidenced on the cumulative probability curve plotted for the growth rate of the metastable pits (Fig. 12c). Some metastable pits formed on the LBM XY sample reached a maximal growth rate value three times higher than metastable pits formed on the wrought and LBM (X,Y)Z samples, in agreement with the median values of the growth rate (Table 5).

Therefore, the cumulative probability curves plotted for all parameters previously defined as characteristic of the metastable pits showed significant differences in the metastable pitting behaviour between the LBM MSS and the wrought one, but also between LBM XY sample and the LBM (X,Y)Z samples. It could be concluded from this statistical analysis that the wrought MSS was characterised by the nucleation of numerous pits which could not reach a stable growth and quickly repassivated, before reaching a high current value, which corresponded to a low amount of dissolved steel. On the contrary, for LBM MSS, the number of metastable pits formed was lower, but the pits

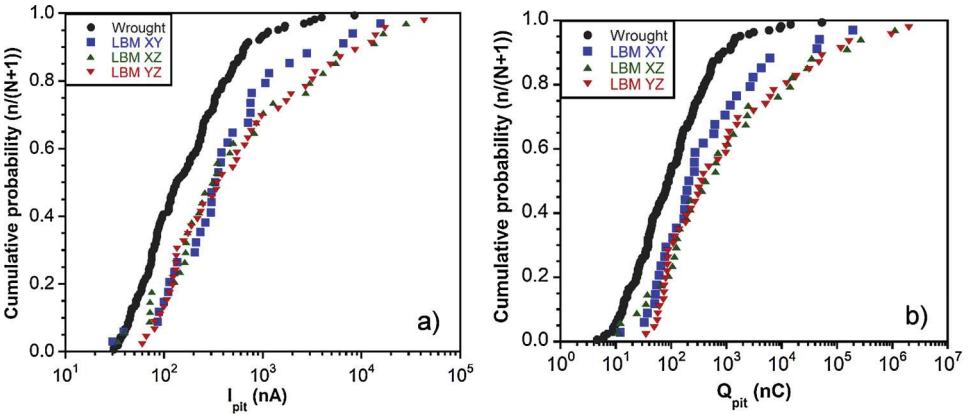

Fig. 11. Cumulative probability distribution of metastable pit a) current (I_{pit}) and b) charge amount (Q_{pit}) for the wrought and LBM 17-4PH MSSs.

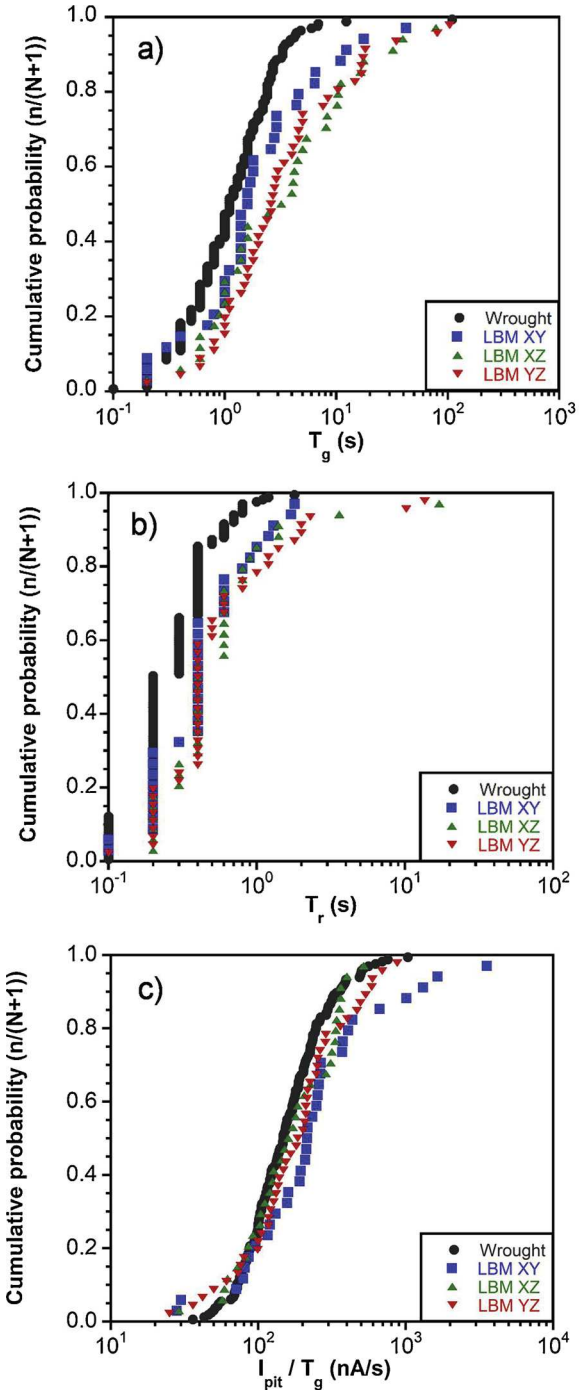

Fig. 12. Cumulative probability distribution of metastable pit a) growth time T_g, b) repassivation time T_r and c) growth rate I_{pit} / T_g.

could propagate for a longer duration time and reached higher maximal current values, which corresponded to a stronger dissolution of the MSS. It could be therefore concluded, in a first approach, that the metastable pits formed for LBM samples were more "stable" than those formed for the wrought MSS. Moreover, results also showed that the LBM XY sample had a specific behaviour compared to the LBM XZ and YZ samples. Indeed, considering the I_{pit}, Q_{pit}, Q_{total}, T_g and T_r values, the LBM XY sample tended to show a metastable pitting behaviour closer to that of the wrought alloy than the LBM XZ and YZ samples; however, it was characterised by higher growth rate values compared to both the wrought MSS and the LBM XZ and YZ samples, even though such values were characteristic of only a few metastable pits, that behave differently than the other pits (Fig. 12c).

Those results could indicate that the wrought MSS would be more resistant to metastable pitting than the LBM MSS, for the same heat treatment (H900), considering in particular the life time of the metastable pits, the I_{pit} and Q_{pit} values. However, the description of the results above showed the complexity of the metastable pitting analysis. One could try to explain this result by referring to the pores present in the LBM samples. Indeed, if the pores were preferential sites for the formation of metastable pits, those pits could grow leading to high current due to the quite confined medium trapped inside the pores. This would be consistent with the higher I_{pit}, Q_{pit}, and T_g values measured for the LBM samples as compared to the wrought MSS. However, considering that the number of stable pits formed near a pore was very low, it was assumed that the passive film would reform inside the pores. Then, to explain that the density of stable pits was similar for LBM and wrought MSSs, while the density of metastable pits was lower for LBM samples compared to the wrought sample, the only robust conclusion the results could support was that the passive films formed on the different samples might be slightly different and therefore might present differences in terms of stability, at least during the first stages of immersion of the samples in the electrolyte. This would be consistent with the i_{pass} values (Fig. 5c, Table 3), showing that the amount of charge used for the growth of the passive film was lower for the LBM MSSs compared to the wrought MSS. This would be also consistent with the conclusions that could be drawn by considering the cumulative probability curves plotted for a last parameter, i.e. the nucleation time of the metastable pits (Fig. 13). These curves clearly showed that, for the LBM XY sample, 80 % of the metastable pits were formed in the first 200 s, whereas, for the wrought MSS, the metastable pits formed during the whole potentiostatic tests. The LBM XZ and YZ samples showed an intermediate behaviour. These results suggested a stronger evolution of the passive films formed on the LBM samples during the immersion in the NaCl solution, compared to the wrought MSS. At the beginning of the immersion, metastable pits could form on the LBM samples, characterised by a high current and long life time, but, after a duration time of immersion, the resistance of the passive films formed on the LBM samples would be better leading to a stop in the initiation of metastable pits. This would be in agreement with the OCP measurements performed (Fig. 5a), that showed that the LBM samples did not reach steady state conditions even after 24 h of immersion contrary to the wrought MSS. This would be also consistent with the shift of E_{pit} toward more positive potentials. Therefore, as said above, the most relevant hypothesis to explain the differences in pitting behaviour of the

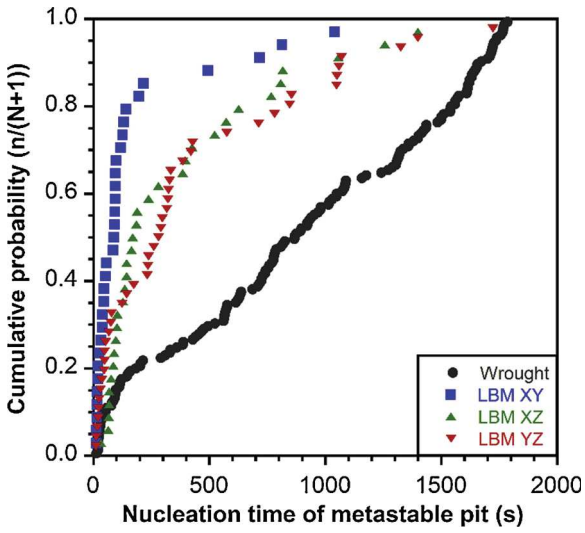

Fig. 13. Cumulative probability distribution of the nucleation time of metastable pits.

wrought and LBM samples was the existence of differences in the composition and / or structure of the passive films. Such results could be related directly to the small differences in chemical composition between the wrought MSS and the LBM MSSs, in particular to the Cr and Ni content, but also to the differences in microstructure previously observed, e.g. austenite / martensite ratio, the lath size and the size and density of Cu-rich precipitates. It is clear that the differences in microstructure are also themselves related, at least for a certain part, to the differences in chemical composition between the two steels. In the same way, the specific behaviour of the LBM XY sample could be interpreted considering in particular the high amount of austenite measured for this sample. Finally, as said previously, the presence of pores inside the LBM samples could not be neglected. Previous results showed that their influence on the stable pitting behaviour of the LBM samples studied here was assumed to be negligible due their very low amount. However, this did not mean that pores could not influence the passive films properties. Indeed, Laleh et al. observed an unexpected low erosion-corrosion resistance for a SLM 316 L SS, as compared to the commercial counterpart; for the authors, even though the pores did not influence the pitting corrosion behaviour, they could modify the repassivation ability of the SS due to chemistry changes inside the pores. Such an analysis could explain the fact that, in the present study, the LBM samples showed more positive E_{pit} values (Fig. 5), but seemed to be less resistant to metastable pitting (Fig. 9 and Table 5), as compared to the wrought MSS. Moreover, the influence of Si-rich oxides inside the pores on the repassivation ability at these sites could be evoked [27], but, at the present time, no experimental data could be given to assess this hypothesis, apart from the fact that TEM observations of Si-rich oxide inclusions (Fig. 4) gave meaning to this hypothesis. Furthermore, Laleh et al. also proposed that residual stresses could contribute to the weak repassivation ability of the SLM 316 L SS [42]. Such a hypothesis was also relevant concerning the LBM samples studied here. Therefore, the results showed that there were several microstructural parameters that could contribute to explain the differences in pitting behaviour observed between all the samples, considering both metastable and stable pitting. Whereas the influence of NbCs on the pitting corrosion behaviour seemed to be clear, much more detailed study is required to evaluate the influence of other microstructural parameters, e.g. the austenite content. Further work is in progress with corrosion tests performed on LBM samples with different heat treatment states related to different microstructures in order to identify the individual role of each metallurgical parameter.

4. Conclusions

The pitting corrosion behaviour of a 17-4PH MSS manufactured by LBM process was investigated in NaCl solution and compared to that of a wrought MSS. The main conclusions are the following:

1 Solution annealing and H900 ageing heat treatments led to a homogeneous microstructure with recrystallised grains for both the wrought and LBM MSSs. However, the LBM MSS had a finer microstructure, with finer martensite laths, finer NbCs precipitates, contained more austenite and more Cu-rich precipitates than the wrought MSS.
2 Polarisation curves plotted in 0.5 M NaCl suggested that the pitting corrosion behaviour of the 17-4PH MSS was improved by the LBM process at the same heat treatment (H900), considering lower i_{pass} and more positive E_{pit} values for the LBM samples compared to the wrought MSS. Results showed a detrimental influence of NbCs on pit initiation; the smaller size of NbCs in the LBM samples could contribute to explain the shift of E_{pit} towards more positive values as compared to the wrought sample. Furthermore, OM observations clearly showed that lack-of-fusion pores were preferential pit initiation sites; however, due to their very low amount in the LBM samples studied, they did not influence their pitting corrosion resistance. The influence of small gas pores was assumed to be negligible.
3 Metastable pits generated on the LBM 17-4PH MSS were very few, characterised by a long life time and a high amount of charge, whereas the wrought MSS presented more metastable pits with short life time and a low amount of charge, which demonstrated significant differences in the metastable pitting behaviour between the LBM and wrought MSSs. Furthermore, for the LBM MSS, a slight difference between XY plane and (X,Y)Z planes reactivity could be also observed. The results were explained by referring to differences in the passive film properties between the different samples, in relation to the differences in microstructure observed. In particular, even though small gas pores seemed to have no influence on stable pit initiation, they were assumed to modify the repassivation ability of the LBM samples.

The results were of main interest for the use of the LBM 17-4PH MSS. Indeed, it seemed that, referring to the stable pitting behaviour of the MSS, the LBM process did not induce any degradation of the properties, and even more it led to a shift of E_{pit} towards more positive values. However, considering the susceptibility of the alloy toward stress corrosion cracking, the results obtained relative to the metastable pitting raised several questions, in particular concerning the influence of the LBM process on the susceptibility to crack initiation.

5. Data availability

The raw/processed data required to reproduce these findings cannot be shared at this time as the data also forms part of an ongoing study.

CRediT authorship contribution statement

Adrien Barroux: Investigation, Formal analysis, Validation, Visualization, Methodology, Data curation, Writing - original draft, Writing - review & editing. **Nadège Ducommun:** Funding acquisition, Resources, Project administration, Supervision, Writing - review & editing. **Eric Nivet:** Funding acquisition, Resources, Project administration, Supervision, Writing - review & editing. **Lydia Laffont:** Methodology, Supervision, Validation, Conceptualization, Data curation, Writing - original draft, Writing - review & editing. **Christine Blanc:** Funding acquisition, Methodology, Project administration, Supervision, Validation, Conceptualization, Data curation, Writing - original draft, Writing - review & editing.

Declaration of Competing Interest

The authors declare that they have no known competing financial interests or personal relationships that could have appeared to influence the work reported in this paper.

Acknowledgement

The authors thank the ANRT for their financial support (Adrien Barroux's PhD thesis).

Appendix A. Supplementary data

Supplementary material related to this article can be found, in the online version, at doi:https://doi.org/10.1016/j.corsci.2020.108594.

References

[1] R. Bhambroo, S. Roychowdhury, V. Kain, V.S. Raja, Effect of reverted austenite on mechanical properties of precipitation hardenable 17-4 stainlesssteel, Mater. Sci. Eng. A 568 (2013) 127–133, https://doi.org/10.1016/j.msea.2013.01.011.
[2] C.N. Hsiao, C.S. Chiou, J.R. Yang, Aging reactions in a 17-4 PH stainless steel,

Mater. Chem. Phys. 74 (2002) 134–142, https://doi.org/10.1016/S0254-0584(01)00460-6.
[3] G. Yeli, M.A. Auger, K. Wilford, G.D.W. Smith, P.A.J. Bagot, M.P. Moody, Sequential nucleation of phases in a 17-4PH steel: microstructural characterisation and mechanical properties, Acta Mater. 125 (2017) 38–49, https://doi.org/10.1016/j.actamat.2016.11.052.
[4] L. Couturier, F. De Geuser, M. Descoins, A. Deschamps, Evolution of the microstructure of a 15-5PH martensitic stainless steel during precipitation hardening heat treatment, Mater. Des. 107 (2016) 416–425, https://doi.org/10.1016/j.matdes.2016.06.068.
[5] H.R. Habibi Bajguirani, C. Servant, G. Cizeron, TEM investigation of precipitation phenomena occurring in PH 15-5 alloy, Acta Metall. Mater. 41 (1993) 1613–1623, https://doi.org/10.1016/0956-7151(93)90270-3.
[6] H.R. Habibi Bajguirani, The effect of ageing upon the microstructure and mechanical properties of type 15-5 PH stainless steel, Mater. Sci. Eng. A 338 (2002) 142–159, https://doi.org/10.1016/S0921-5093(02)00062-X.
[7] R. Kapoor, I.S. Batra, On the α′ to γ transformation in maraging (grade 350), PH 13-8 Mo and 17-4 PH steels, Mater. Sci. Eng. A 371 (2004) 324–334, https://doi.org/10.1016/j.msea.2003.12.023.
[8] A. Abbasi Aghuy, M. Zakeri, M.H. Moayed, M. Mazinani, Effect of grain size on pitting corrosion of 304L austenitic stainless steel, Corros. Sci. 94 (2015) 368–376, https://doi.org/10.1016/j.corsci.2015.02.024.
[9] J. Wang, H. Zou, C. Li, S. Qiu, B. Shen, The effect of microstructural evolution on hardening behavior of type 17-4PH stainless steel in long-term aging at 350 °C, Mater. Charact. 57 (2006) 274–280, https://doi.org/10.1016/j.matchar.2006.02.004.
[10] H. Mirzadeh, A. Najafizadeh, Aging kinetics of 17-4 PH stainless steel, Mater. Chem. Phys. 116 (2009) 119–124, https://doi.org/10.1016/j.matchemphys.2009.02.049.
[11] U.K. Viswanathan, S. Banerjee, R. Krishnan, Effects of aging on the microstructure of 17-4 PH stainless steel, Mater. Sci. Eng. A 104 (1988) 181–189, https://doi.org/10.1016/0025-5416(88)90420-X.
[12] T. DebRoy, H.L. Wei, J.S. Zuback, T. Mukherjee, J.W. Elmer, J.O. Milewski, A.M. Beese, A. Wilson-Heid, A. De, W. Zhang, Additive manufacturing of metallic components – process, structure and properties, Prog. Mater. Sci. 92 (2018) 112–224, https://doi.org/10.1016/j.pmatsci.2017.10.001.
[13] H. Fayazfar, M. Salarian, A. Rogalsky, D. Sarker, P. Russo, V. Paserin, E. Toyserkani, A critical review of powder-based additive manufacturing of ferrous alloys: process parameters, microstructure and mechanical properties, Mater. Des. 144 (2018) 98–128, https://doi.org/10.1016/j.matdes.2018.02.018.
[14] F. Huber, C. Bischof, O. Hentschel, J. Heberle, J. Zettl, K. Yu, Nagulin, M. Schmidt, Laser beam melting and heat-treatment of 1.2343 (AISI H11) tool steel – microstructure and mechanical properties, Mater. Sci. Eng. A 742 (2019) 109–115, https://doi.org/10.1016/j.msea.2018.11.001.
[15] A. Kudzal, B. McWilliams, C. Hofmeister, F. Kellogg, J. Yu, J. Taggart-Scarff, J. Liang, Effect of scan pattern on the microstructure and mechanical properties of powder bed fusion additive manufactured 17-4 stainless steel, Mater. Des. 133 (2017) 205–215, https://doi.org/10.1016/j.matdes.2017.07.047.
[16] H. Gu, H. Gong, D. Pal, K. Rafi, T. Starr, B. Stucker, Influences of energy density on porosity and microstructure of selective laser melted 17-4PH stainless steel, 2013 Solid Freeform Fabrication Symposium (2013) 474.
[17] L.E. Murr, E. Martinez, J. Hernandez, S. Collins, K.N. Amato, S.M. Gaytan, P.W. Shindo, Microstructures and properties of 17-4 PH stainless steel fabricated by selective laser melting, J. Mater. Res. Technol. 1 (2012) 167–177, https://doi.org/10.1016/S2238-7854(12)70029-7.
[18] S.D. Meredith, J.S. Zuback, J.S. Keist, T.A. Palmer, Impact of composition on the heat treatment response of additively manufactured 17–4 PH grade stainless steel, Mater. Sci. Eng. A 738 (2018) 44–56, https://doi.org/10.1016/j.msea.2018.09.066.
[19] S. Cheruvathur, E.A. Lass, C.E. Campbell, Additive manufacturing of 17-4 PH stainless steel: post-processing heat treatment to achieve uniform reproducible microstructure, JOM 68 (2016) 930–942, https://doi.org/10.1007/s11837-015-1754-4.S.
[20] A. Yadollahi, N. Shamsaei, S.M. Thompson, A. Elwany, L. Bian, Mechanical and microstructural properties of selective laser melted 17-4 PH stainless steel, ASME 2015 International Mechanical Engineering Congress and Exposition, American Society of Mechanical Engineers, 2015, https://doi.org/10.1115/IMECE2015-52362.
[21] A. Yadollahi, N. Shamsaei, S.M. Thompson, A. Elwany, L. Bian, Effects of building orientation and heat treatment on fatigue behavior of selective laser melted 17-4 PH stainless steel, Int. J. Fatigue 94 (Part 2) (2017) 218–235, https://doi.org/10.1016/j.ijfatigue.2016.03.014.
[22] T. Lebrun, K. Tanigaki, K. Horikawa, H. Kobayashi, Strain rate sensitivity and mechanical anisotropy of selective laser melted 17-4 PH stainless steel, Mech. Eng. J. 1 (2014), https://doi.org/10.1299/mej.2014smm0049.
[23] T. LeBrun, T. Nakamoto, K. Horikawa, H. Kobayashi, Effect of retained austenite on subsequent thermal processing and resultant mechanical properties of selective laser melted 17–4 PH stainless steel, Mater. Des. 81 (2015) 44–53, https://doi.org/10.1016/j.matdes.2015.05.026.
[24] F. Hengsbach, P. Koppa, K. Duschik, M.J. Holzweissig, M. Burns, J. Nellesen, W. Tillmann, T. Tröster, K.-P. Hoyer, M. Schaper, Duplex stainless steel fabricated by selective laser melting - microstructural and mechanical properties, Mater. Des. 133 (2017) 136–142, https://doi.org/10.1016/j.matdes.2017.07.046.
[25] R. Rashid, S.H. Masood, D. Ruan, S. Palanisamy, R.A. Rahman Rashid, M. Brandt, Effect of scan strategy on density and metallurgical properties of 17-4PH parts printed by Selective Laser Melting (SLM), J. Mater. Process. Technol. 249 (2017) 502–511, https://doi.org/10.1016/j.jmatprotec.2017.06.023.
[26] Y. Sun, R.J. Hebert, M. Aindow, Non-metallic inclusions in 17-4PH stainless steel parts produced by selective laser melting, Mater. Des. 140 (2018) 153–162, https://doi.org/10.1016/j.matdes.2017.11.063.
[27] X. Lou, P.L. Andresen, R.B. Rebak, Oxide inclusions in laser additive manufactured stainless steel and their effects on impact toughness and stress corrosion cracking behavior, J. Nucl. Mater. 499 (2018) 182–190, https://doi.org/10.1016/j.jnucmat.2017.11.036.
[28] D. Kong, X. Ni, C. Dong, L. Zhang, C. Man, J. Yao, K. Xiao, X. Li, Heat treatment effect on the microstructure and corrosion behavior of 316L stainless steel fabricated by selective laser melting for proton exchange membrane fuel cells, Electrochim. Acta 276 (2018) 293–303, https://doi.org/10.1016/j.electacta.2018.04.188.
[29] S.-Y. Lu, K.-F. Yao, Y.-B. Chen, M.-H. Wang, N. Chen, X.-Y. Ge, Effect of quenching and partitioning on the microstructure evolution and electrochemical properties of a martensitic stainless steel, Corros. Sci. 103 (2016) 95–104, https://doi.org/10.1016/j.corsci.2015.11.010.
[30] S.S.M. Tavares, F.J. da Silva, C. Scandian, G.F. da Silva, H.F.G. de Abreu, Microstructure and intergranular corrosion resistance of UNS S17400 (17-4PH) stainless steel, Corros. Sci. 52 (2010) 3835–3839, https://doi.org/10.1016/j.corsci.2010.07.016.
[31] H. Luo, Q. Yu, C. Dong, G. Sha, Z. Liu, J. Liang, L. Wang, G. Han, X. Li, Influence of the aging time on the microstructure and electrochemical behaviour of a 15-5PH ultra-high strength stainless steel, Corros. Sci. 139 (2018) 185–196, https://doi.org/10.1016/j.corsci.2018.04.032.
[32] V. Vignal, S. Ringeval, S. Thiébaut, K. Tabalaiev, C. Dessolin, O. Heintz, F. Herbst, R. Chassagnon, Influence of the microstructure on the corrosion behaviour of low-carbon martensitic stainless steel after tempering treatment, Corros. Sci. 85 (2014) 42–51, https://doi.org/10.1016/j.corsci.2014.03.036.
[33] P. Marcus, V. Maurice, H.-H. Strehblow, Localized corrosion (pitting): a model of passivity breakdown including the role of the oxide layer nanostructure, Corros. Sci. 50 (2008) 2698–2704, https://doi.org/10.1016/j.corsci.2008.06.047.
[34] D. Nakhaie, M.H. Moayed, Pitting corrosion of cold rolled solution treated 17-4 PH stainless steel, Corros. Sci. 80 (2014) 290–298, https://doi.org/10.1016/j.corsci.2013.11.039.
[35] M. Ziętala, T. Durejko, M. Polański, I. Kunce, T. Płociński, W. Zieliński, M. Łazińska, W. Stępniowski, T. Czujko, K.J. Kurzydłowski, Z. Bojar, The microstructure, mechanical properties and corrosion resistance of 316L stainless steel fabricated using laser engineered net shaping, Mater. Sci. Eng. A 677 (2016) 1–10, https://doi.org/10.1016/j.msea.2016.09.028.
[36] X. Chen, J. Li, X. Cheng, H. Wang, Z. Huang, Effect of heat treatment on microstructure, mechanical and corrosion properties of austenitic stainless steel 316L using arc additive manufacturing, Mater. Sci. Eng. A 715 (2018) 307–314, https://doi.org/10.1016/j.msea.2017.10.002.
[37] W.K. Chan, C.T. Kwok, K.H. Lo, Effect of laser surface melting and subsequent re-aging on microstructure and corrosion behavior of aged S32950 duplex stainless steel, Mater. Chem. Phys. 207 (2018) 451–464, https://doi.org/10.1016/j.matchemphys.2018.01.007.
[38] M.J.K. Lodhi, K.M. Deen, W. Haider, Corrosion behavior of additively manufactured 316L stainless steel in acidic media, Materialia 2 (2018) 111–121, https://doi.org/10.1016/j.mtla.2018.06.015.
[39] W.S.W. Harun, R.I.M. Asri, F.R.M. Romlay, S. Sharif, N.H.M. Jan, F. Tsumori, Surface characterisation and corrosion behaviour of oxide layer for SLMed-316L stainless steel, J. Alloys. Compd. 748 (2018) 1044–1052, https://doi.org/10.1016/j.jallcom.2018.03.233.
[40] Q. Chao, V. Cruz, S. Thomas, N. Birbilis, P. Collins, A. Taylor, P.D. Hodgson, D. Fabijanic, On the enhanced corrosion resistance of a selective laser melted austenitic stainless steel, Scr. Mater. 141 (2017) 94–98, https://doi.org/10.1016/j.scriptamat.2017.07.037.
[41] M.J. Tobar, J.M. Amado, J. Montero, A. Yáñez, A study on the effects of the use of gas or water atomized AISI 316L steel powder on the corrosion resistance of laser deposited material, Phys. Procedia 83 (2016) 606–612, https://doi.org/10.1016/j.phpro.2016.08.063.
[42] M. Laleh, A.E. Hughes, W. Xu, I. Gibson, M.Y. Tan, Unexpected erosion-corrosion behaviour of 316L stainless steel produced by selective laser melting, Corros. Sci. 155 (2019) 67–74, https://doi.org/10.1016/j.corsci.2019.04.028.
[43] R.N. Clark, J. Searle, T.L. Martin, W.S. Walters, G. Williams, The role of niobium carbides in the localised corrosion initiation of 20Cr-25Ni-Nb advanced gas-cooled reactor fuel cladding, Corros. Sci. 165 (2020) 108365, , https://doi.org/10.1016/j.corsci.2019.108365.
[44] M.A. Melia, H.-D.A. Nguyen, J.M. Rodelas, E.J. Schindelholz, Corrosion properties of 304L stainless steel made by directed energy deposition additive manufacturing, Corros. Sci. 152 (2019) 20–30, https://doi.org/10.1016/j.corsci.2019.02.029.
[45] M. Laleh, A.E. Hughes, S. Yang, J. Li, W. Xu, I. Gibson, M.Y. Tan, Two and three-dimensional characterisation of localised corrosion affected by lack-of-fusion pores in 316L stainless steel produced by selective laser melting, Corros. Sci. 165 (2020) 108394, , https://doi.org/10.1016/j.corsci.2019.108394.
[46] M. Laleh, A.E. Hughes, W. Xu, P. Cizek, M.Y. Tan, Unanticipated drastic decline in pitting corrosion resistance of additively manufactured 316L stainless steel after high-temperature post-processing, Corros. Sci. 165 (2020) 108412, , https://doi.org/10.1016/j.corsci.2019.108412.
[47] P.C. Pistorius, G.T. Burstein, Growth of corrosion pits on stainless steel in chloride solution containing dilute sulphate, Corros. Sci. 33 (1992) 1885–1897, https://doi.org/10.1016/0010-938X(92)90191-5.
[48] G.T. Burstein, P.C. Pistorius, S.P. Mattin, The nucleation and growth of corrosion pits on stainless steel, Corros. Sci. 35 (1993) 57–62, https://doi.org/10.1016/0010-938X(93)90133-2.
[49] S. Pahlavan, S. Moazen, I. Taji, K. Saffar, M. Hamrah, M.H. Moayed, S. Mollazadeh Beidokhti, Pitting corrosion of martensitic stainless steel in halide bearing solutions, Corros. Sci. 112 (2016) 233–240, https://doi.org/10.1016/j.corsci.2016.07.008.